VSP

Journal of Adhesion Science and Technology 23 (2009) 1303–1325

Journal of ADHESION SCIENCE and TECHNOLOGY
www.brill.nl/jast

Variation of the Electrostatic Adhesion Force on a Rough Surface due to the Deformation of Roughness Asperities During Micromanipulation of a Spherical Rigid Body

M. Sausse Lhernould [a], P. Berke [b], T. J. Massart [b], S. Régnier [c] and P. Lambert [a,*]

[a] Université Libre de Bruxelles (ULB), Av. F. D. Roosevelt 50, B-1050 Bruxelles, BEAMS CP165/56, Belgium

[b] Université Libre de Bruxelles (ULB), Av. F. D. Roosevelt 50, B-1050 Bruxelles, BATir Dept. CP 194/2, Belgium

[c] ISIR, Université Pierre et Marie Curie (UPMC), 18 route du Panorama, BP 61, 92265 Fontenay-aux-Roses, France

Received in final form 26 February 2009

Abstract

The micromanipulation of objects of size between 10 μm and 1 mm is often disturbed by the adhesion between the contacting surfaces. The electrostatic force in the contact alone can significantly perturb the micromanipulation by its important adhesion effect. The electrostatic adhesion force is influenced by many factors, i.e., the materials of the contacting bodies and the topography of the contact surface. Micromanipulation by contact involves applying a squeezing force to hold the object firmly which causes the contact surface to deform, flattening the surface asperities. The prime purpose of this work is to study the influence of the plastic deformation of the surface asperities on the electrostatic adhesion force considering the contact between two conductors. A single-level model of the surface roughness was considered in this study, approximating the shape of a surface asperity by a sine function. A simulation tool based on the finite element method was used to compute the elastic–plastic deformation of the model surface asperities during micromanipulation. Another numerical model was used to compute the electrostatic adhesion force acting on the surface asperities in the initial and in the deformed configurations. A magnification factor of up to 20 was obtained for the electrostatic force in the contact evaluated numerically, related to the flattening of the surface asperities, which can potentially lead to perturbations when releasing the object. The observed effect is merely a lower bound of the real one, considering the simplifying assumptions of the numerical models.

Keywords

Microscale manipulation, electrostatic force, surface roughness, finite deformation, numerical simulation, contact

* To whom correspondence should be addressed. Tel.: +32 2 650 4244; Fax: +32 2 6502482; e-mail: pierre.lambert@ulb.ac.be

 DOI:10.1163/156856109X434026

1. Introduction

A new field of interest which has emerged recently from the development of micro-electro-mechanical systems (MEMS) is the use of (coated) metallic materials for surgical applications because of their possible bio-compatibility and interesting mechanical and wear properties compared to the widely used silicon. Surface phenomena, such as adhesion, play a significant role in MEMS devices, with often disturbing effects leading to a short lifespan of these micro-machines involving moving parts [1, 2]. It is, therefore, a general objective of the related field of research to study the surface forces responsible for these perturbations which, although negligible on the macroscopic scale, are of great importance on the considered small scales. This originates from the different ratio between surface and volume forces when considering the microscale/nanoscale: the surface-to-volume ratio is indeed much more important on small scales.

In this study, issues related to electrostatic contact adhesion after micromanipulation by contact with a gripper made of pure nickel are investigated through a fully numerical approach. Surface forces, particularly adhesion [3], play a dominant role in micromanipulation by contact and in the handling of microdevices and components [4, 5]. The disturbing adhesion between the manipulating equipment and the object can lead to the impossibility of the release and precise positioning of the handled object. Various surface forces with different physics involved can be identified as potential sources of adhesion, i.e., the capillary force [6, 7], the van der Waals force [7, 8], the electrostatic force [9] and the chemical bonding of surfaces.

This work focuses on the contribution of only the electrostatic force to adhesion because it is the most significant for grasping and manipulating objects of the considered size [10], and since its magnitude is such that it alone can be important enough to perturb the manipulation of micro-objects. This long-range force is active for separation distances in the order of the radius of the manipulated object.

A significant decrease in the magnitude of surface forces was observed due to the presence of surface roughness [11–13]. In micromanipulation the handled object is in contact with the gripper and it is unavoidable that the surface asperities on the contacting surfaces are crushed, to some extent, due to the applied grasping force. The resulting change in the surface topography by the flattening of the surface asperities during micromanipulation can give rise to an increase in the contact adhesion. The prime purposes of this work are to contribute to the understanding of how the induced deformation of the contacting rough surfaces influences the electrostatic adhesion force and to gain some insight into the physics of the evolution of electrostatic adhesion during micromanipulation by an adapted multi-physics computation. Our intention is to show that incorporating the plastic deformation of the surface roughness in the study of the contact adhesion can account for a significant increase in electrostatic adhesion, which can be responsible for experimental release problems.

The computational work can be divided into two parts, coupled unilaterally. The first one involves the computation of the elastic–plastic deformation of surface asperities during micromanipulation. The second part aims at the evaluation of the variation of the electrostatic contact adhesion during micromanipulation, based on the deformation of the surface asperities using an electrostatic numerical model. This unilateral coupling of the electrostatic simulations introduces the assumption that the electrostatic force levels are much smaller than the ones necessary to deform the surface asperities, therefore, the electrostatic forces and their variations do not influence the deformation obtained (this will be confirmed later). This assumption is not obviously verified for all mechanical phenomena, since electrostatic forces can have an influence on the frictional behavior of a surface, for example [14]. The electrostatic adhesion forces on the surface asperities in the initial, undeformed and in the final, deformed configurations are calculated and compared to evaluate the variation of their magnitude during micromanipulation.

This study is presented as follows. Section 2 deals with the mechanical problem of the deformation of the gripper arm during micromanipulation on the scale of the object (the macroscale) and on the scale of the surface roughness asperities (the microscale). In Section 3 the results of the electrostatic simulations valid for the microscale are presented and discussed. Based on the numerical results, analytical models using simple geometrical approximations are set up for the evaluation of electrostatic adhesion force in the initial and the deformed configurations of the surface asperities. Section 4 brings a discussion on the assumptions used in this study and on their implication on the results and trends obtained, explaining why the computed increase in the electrostatic adhesion force due to the plastic deformation of the surface asperities is believed to be a lower bound of the one experienced in real-life applications. The outlook of this study is presented in Section 4 as well.

2. Contact Deformation Modeling

This part of the work addresses the problem of the evaluation of the deformation of a gripper arm made of pure nickel during manipulation. Two numerical models were set up on two different scales for this purpose. A macroscale contact model (Section 2.1) applicable to the scale of the manipulated object was used to evaluate the deformation of the gripper arm when realistic squeezing force levels are applied to grab spherical objects with sizes ranging from 10 μm to 1 mm. The magnitude of the obtained macroscopic deformation gave an indication for the deformation levels to be applied in the microscale contact model applicable to the level of the surface roughness asperities.

A microscale model (Section 2.2) was used to determine the deformed shapes of the model roughness asperities considering the chosen deformation level. The results of the microscale model were the input data for the electrostatic simulations

that determine the electrostatic adhesion force in the contact. This separation of scales was adopted to allow computing the considered problem.

2.1. Macroscale Contact Model of Micromanipulation: Surface Roughness Deformation Estimate

This numerical model is set up on the scale of the manipulated object, which was assumed to have a perfect spherical geometry with a radius varying in the range of sizes of the potentially manipulated objects $R_{\text{obj}} = [10\ \mu\text{m}, \ldots, 1\ \text{mm}]$ [15]. For the sake of simplicity and computational efficiency the roughness of both the surfaces of the gripper arm and the manipulated object was neglected on the macroscale.

The gripper arm was considered to be made of pure nickel and was modeled as a deformable body having a perfectly flat frictionless contact surface. Frictional effects were not taken into account in this study in order to reduce the complexity of the numerical models and to ensure computational efficiency.

In the numerical model an isotropic rate-independent hardening behavior of pure nickel, obeying Ludwik's equation (1), was assumed.

$$\sigma_{\text{v}} = \sigma_0 + K\kappa^n, \tag{1}$$

where σ_{v} (MPa) stands for the current yield limit, σ_0 (MPa) the initial yield stress, K (MPa) the hardening coefficient, κ a measure of cumulative plastic strain and n the hardening exponent of pure nickel. The elastic–plastic parameters of the model were calculated to fit the experimental stress–strain curve extracted from uniaxial tension measurements on polycrystalline pure nickel [16]. The considered parameter set for the pure nickel material was: the Young's modulus $E = 207$ GPa, the Poisson's coefficient $\nu = 0.31$ and $\sigma_0 = 59$ MPa, $K = 1165$ MPa, $n = 0.56$. The obtained elastic and plastic parameters set was compared with other works [17–21] reporting data on the hardening behavior of pure nickel and were found to be in good agreement.

The manipulated spherical object was considered to be undeformable and was modeled by a rigid body (this assumption will be validated later).

The applied squeezing force varied in the range of the real manipulation force $F = [1\ \text{mN}, \ldots, 600\ \text{mN}]$ [15]. Considering the symmetry of the problem the finite element meshes were two-dimensional (Fig. 1) and were built from 8 noded elastic–plastic axisymmetric elements capable of handling finite deformations. The models consisted of more than 33 500 degrees of freedom to be able to reproduce with high precision the stress and plastic strain evolutions during the simulation. In the simulation the side nodes of the mesh were constrained in the horizontal direction, the deformable body was constrained to move upwards to come into contact with the rigid object, for which a fixed position in space was assumed. The nodes on the bottom side of the model were not constrained in the horizontal direction. The geometrical size of the meshes in all cases was chosen sufficiently large such that a homogeneous stress distribution at the boundary of the model was obtained. A finite

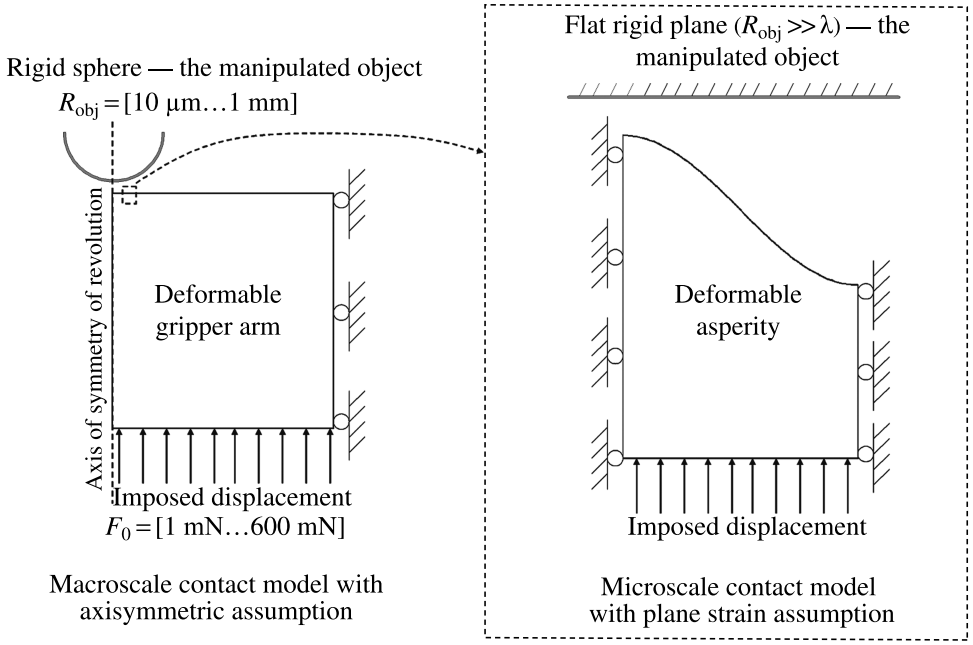

Figure 1. The two considered contact models set up on different scales. Left: macroscale model of the micromanipulation considering realistic loading conditions and an axisymmetric description with the manipulated object modeled as a rigid (undeformable) body. F_0 is the manipulating force, R_{obj} the radius of the manipulated object. Right: microscale contact model of the flattening of one surface asperity on the surface of the gripper arm, using a plain strain assumption. λ is the wavelength of the sine function describing the asperity shape, the manipulated object is modeled as a rigid fiat plane.

element code was used for the simulation of the mechanical deformation in a contact setting. Unilateral contact constraints on the contact interface were taken into account using the high-precision augmented Lagrangian method with a Newton-type continuous multiplier update procedure [22]. A finite deformation framework based on the corotational formulation [23] was used, which has the advantage to be capable of handling arbitrary large rigid rotations.

Two extreme contact configurations were analyzed on the macro-level:

Case A. The largest manipulated object with $R_{max} = 1$ mm was combined with the smallest manipulation force $F_0^{min} = 1$ mN. This macroscopic contact generates the lowest contact stresses and corresponds to the least severe loading conditions. The behavior of the material remains mainly elastic, with a contact area radius of $a_{macro} = 1.653$ μm close to the elastic contact radius approximated by the theory of Hertz [24]. The obtained penetration of the rigid body was $h_{macro} = 2.3$ nm.

Case B. The smallest object with $R_{min} = 10$ μm was manipulated with the largest force level $F_0^{max} = 600$ mN. In this case the contact response was dominated by

the plastic deformation of the gripper arm due to the high contact stresses. The calculated macroscopic contact radius was $a_{\text{macro}} = 10$ μm, almost 4 times that based on the elastic approximation by the theory of Hertz. The penetration of the rigid body was also strongly increased and became comparable to the radius of the sphere with $h_{\text{macro}} = 10$ μm.

In both theoretical contact cases studied the finite deformation of the gripper arm was observed. In micromanipulation it is necessary to squeeze objects in order to hold them firmly. Case A, taking the largest object with the smallest gripping force most probably gives a lower bound to the contact stresses and the deformation of the gripper arm in the macroscale model with respect to the real configuration.

2.2. Microscale Rough Contact Model

In the present investigation numerical simulations are used to obtain the exact solution of the semi-coupled mechanical–electrostatic problem on the microscale, since no analytical solution is available. This allows to evaluate the influence of the plastic deformation of the surface roughness on electrostatic contact adhesion. The objective of this section is the modeling of the elastic–plastic deformation of the surface asperities on the gripper arm during micromanipulation. For this purpose, a numerical model was defined on the scale of the surface roughness asperities, i.e., on the microscale.

A brief review of the rough surface models is presented in order to provide motivation for the choice of the surface roughness representation used here. The roughness of a real surface has a multi-level nature calling for multi-scale descriptions in the numerical models. In a most general fashion a roughness profile can be considered as the convolution of single profiles with various wavelengths and different amplitude to wavelength ratios. The description of the experimentally observed surface roughness in a numerical model depends on the physics involved.

Some numerical works considering rough surface contact address the problem of cross-property connections [25], such as the variation of contact conductance [26]. Most frequently, in the mechanical simulation of rough surface deformation, a purely elastic response of the material is considered [25, 27]; and depending on the modeled problem a fair agreement between experimental and numerical results can be found. One family of models considers a single-level or multi-level description using asperities with statistical height distribution, such as initially proposed in [28]. Another type of model uses the fractal description of the surface roughness. The latter has been applied, for example, to the surface of polycrystalline Si for MEMS applications [29, 30] and for ns-C films [31]. Some complementary approaches to the present work should be mentioned, in which semi-analytical methods were used to evaluate the deformation of the surface roughness and the contact adhesion with a fractal description, with the assumption of a perfectly plastic material behavior [32, 33].

Unlike these works, the approach presented here is fully computational, and incorporates an experimentally measured material hardening behavior, as well as the explicit computation of the plastic deformation of the model surface asperities. This approach is thus complementary to the previous works. It avoids *a priori* postulated assumptions regarding the plastic behavior of the material, but due to computational limitations a fractal description of the surface roughness cannot be adopted in the present numerical scheme, which implies the use of a more simple roughness representation.

The surface roughness was chosen to have the simplest representation here, approximated by a sine function $y_i(x) = A_i \sin(2\pi/\lambda_i x)$, considering only the first level of a protuberance-on-protuberance type roughness description, as in [34–36]. This model has the advantage to be easily adaptable to studies for multi-level representations, in which the shape of the surface asperities may change at different levels, or for a fractal description. Note that the use of this single-level representation in the present investigation results in a higher bound to the initial electrostatic adhesion force in the contact. Indeed, the higher order roughness present in self-similar descriptions was neglected here. As a result, the initial contact surface was larger than in the case of real surfaces, which yielded a higher electrostatic force (as explained in Section 3). From the point of view of electrostatic simulations, the same choice of a sinusoidal representation of the geometry was made in [37] to compute the electrostatic repulsive energy between two rough colloidal particles.

For the sake of simplicity the amplitude A_i and the wavelength λ_i of each asperity i of the surface roughness composed of n interconnected asperities were defined to be the same in this study. The response of the surface roughness to deformation was shown experimentally to depend on the shape of the roughness asperities [31]. In order to cover a large range of roughness asperity shapes considering their sinusoidal description, the ratio between the amplitude and the wavelength of the sine function was varied. In the model the wavelength of the asperities was kept constant $\lambda_i = \lambda = 200$ nm and 13 different values of the amplitude (Table 1) were chosen in the range $A_i/\lambda = [0.01, \ldots, 0.85]$ from the bluntest to the sharpest profiles (Fig. 2).

The assumption that the size of the manipulated object is much larger than the wavelength of the roughness profiles, i.e.,

$$R_{\text{obj}} = [10\ \mu\text{m}, \ldots, 1\ \text{mm}] \gg \lambda = 200\ \text{nm} \tag{2}$$

on the microscale generally holds for the majority of practical cases [38]. As a consequence, in view of equation (2) some simplifying assumptions could be applied to the microscale numerical contact model, such as (i) the contact radius of the manipulated object was considered to be infinite and this object was thus modeled as a rigid flat plane on this scale and (ii) the neighboring roughness peaks were assumed to deform homogeneously in the vicinity of a chosen roughness asperity.

If every roughness peak is assumed to deform in the same way on the considered scale, as performed in [39], the characterization of the behavior of one rough-

Table 1.
Studied roughness shapes and related results. A_i is the initial amplitude, $\lambda = 200$ nm the wavelength, d_i the prescribed flattening of the asperities, R_i the generated reaction force per roughness peak, l_i^{peak} and l_i^{unload} are the plateau lengths at peak load and in the unloaded configuration, respectively. F_{init}, $F_{\text{def}}^{\text{peak}}$ and $F_{\text{def}}^{\text{unload}}$ stand for the electrostatic force on the asperity for the initial shape, for the deformed shape at peak load and for the deformed shape in the unloaded configurations, respectively, for a potential difference of 0.1 V

i	1	2	3	4	5	6	7	8	9	10	11	12	13
A_i/λ	0.01	0.03	0.05	0.10	0.15	0.20	0.25	0.35	0.45	0.55	0.65	0.75	0.85
A_i (nm)	2	6	10	20	30	40	50	70	90	110	130	150	170
d_i (nm)	1.34	4	6.67	13.34	20	26.67	33.34	46.67	60	73.34	86.67	100	113.34
R_i (μN)	0.0320	0.0530	0.0696	0.0970	0.1132	0.1198	0.1212	0.1184	0.1158	0.1154	0.1156	0.1168	0.1178
l_i^{peak} (nm)	76.2	77.2	80.1	84.6	85.6	87.6	87	81.4	75	72.8	69.6	68.2	67.2
l_i^{unload} (nm)	69.8	69	70.2	65.8	63	64	66.2	66.2	63	58.8	57.8	55.4	54.8
F_{init} (mN/m)	9.1	5.1	3.9	2.8	2.3	1.9	1.7	1.5	1.3	1.1	1.0	1.0	0.9
$F_{\text{def}}^{\text{peak}}$ (mN/m)	24.6	23.3	23.5	24.0	24.6	24.8	24.6	23.1	21.5	20.8	20.1	19.7	19.4
$F_{\text{def}}^{\text{unload}}$ (mN/m)	22.8	21.4	21.3	21.1	21.2	21.4	21.4	20.4	19.1	18.3	17.7	17.3	17.0

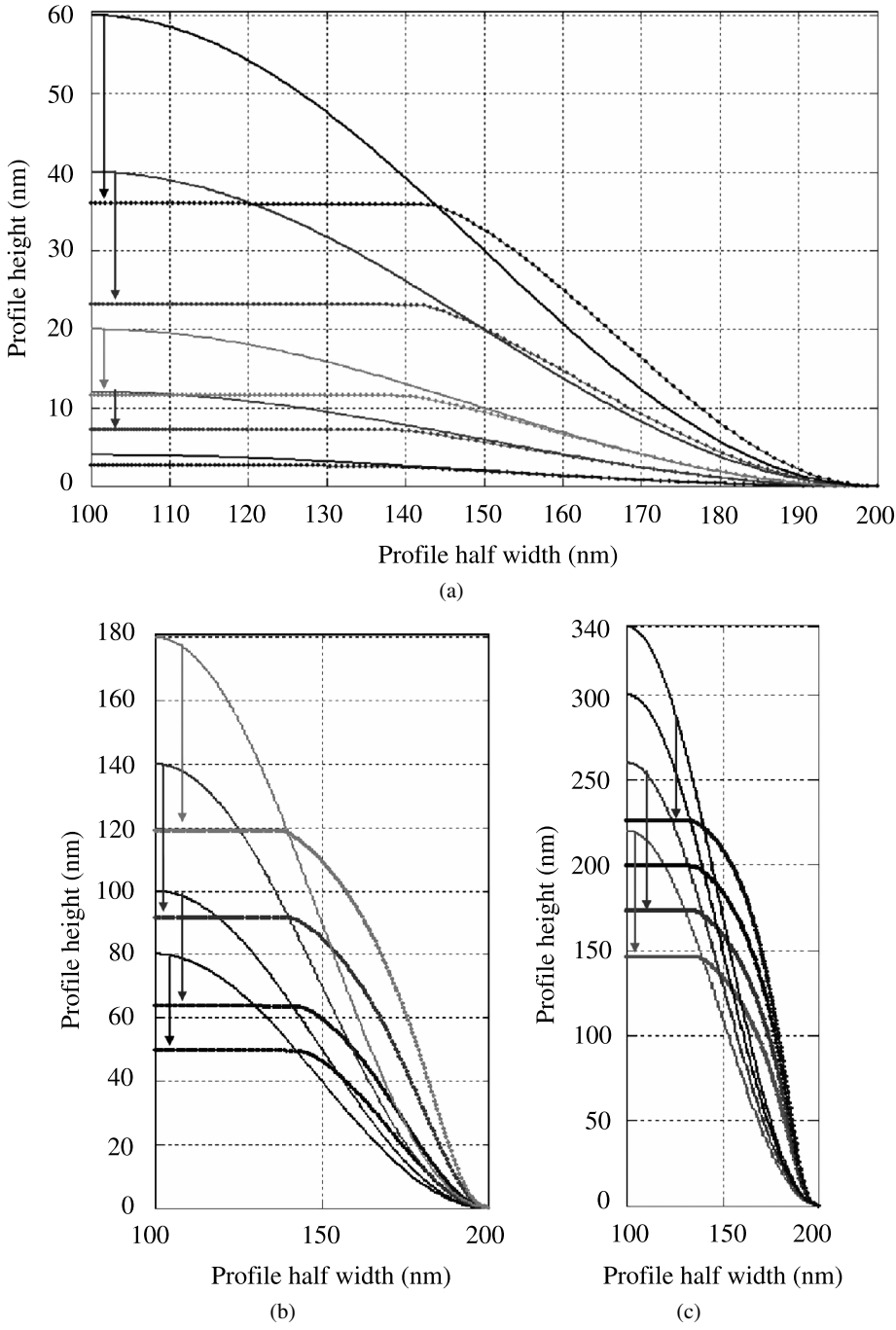

Figure 2. Studied surface asperity shapes in the initial and in the deformed configurations. (a) Blunt asperities $A/\lambda = [0.01, \ldots, 0.15]$. (b) Sharper asperity shapes $A/\lambda = [0.2, \ldots, 0.45]$. (c) Sharpest asperity shapes $A/\lambda = [0.55, \ldots, 0.85]$.

ness peak is sufficient using a periodicity condition. This is a common practice to achieve a reasonable computational efficiency in numerical models of a rough surface contact [30, 40]. Note that the results of some experimental and numerical works investigating the difference in the responses of single and multi-asperity contacts on small scales showed that this assumption may alter the overall response of the contact, particularly for cases when the contact penetration is comparable to the height of the asperities [31, 39, 41–43]. Considering the finite deformation of the gripper arm on the macroscale with realistic loading conditions, the flattening d_i of a modeled roughness asperity i in the microscale model using the periodicity condition was chosen to be $d_i/A_i = 2/3$ corresponding to a moderate deformation on the scale of the surface roughness.

This set of assumptions, based on equation (2), on the microscale thus introduces the assumption of a full separation of the length scales of the manipulated object (the macroscale) from those defining the conditions of the contact between the roughness peak and the object (the microscale), as shown in Fig. 1.

In the microscale numerical model the geometry was two-dimensional with a plane strain assumption. Only the half of the sinusoidal profile was considered due to the symmetry of its shape. All 13 finite element meshes with different A_i values were built from 8 noded elastic–plastic finite deformation elements in the corotational finite deformation description with more than 14 800 degrees of freedom. The geometrical size of the meshes was chosen such that a homogeneous stress distribution was found on the bottom side of the model. The left and right sides of the deformable body were constrained in the horizontal direction in order to represent the above-mentioned periodicity condition. The bottom side of the body was free in the horizontal direction and moved upwards in the vertical direction by a value of $d_i = 2A_i/3$ (the imposed flattening) using a displacement-controlled simulation. Unilateral contact conditions without friction were used between the contact nodes on the top side of the deformable body and a rigid horizontal plane representing the manipulated object. The same elastic–plastic rate-independent constitutive law with isotropic hardening was used for the nickel deformable body as before.

In a contact setting, both contacting objects often suffer both elastic and plastic deformations due to the high contact stresses. The assumption that the handled object can be considered undeformable was verified to be valid. This was achieved by simulating the microscale contact problem with a deformable object made of S45C carbon steel ($E^{\mathrm{S45C}} = 205$ GPa, $\sigma_0^{\mathrm{S45C}} = 400$ MPa). Indeed, the plastic deformation was found to take place only at the nickel roughness peak, because of the lower elastic limit of pure nickel. In the contact considered although the elastic properties of both materials were similar, due to its lower yield limit, pure nickel reached the plastic domain, while the carbon steel was still showing an elastic contact response. Moreover, the elastic deformation of the carbon steel object was also confirmed to be negligible. The rigid body modeling of the handled object thus appears rea-

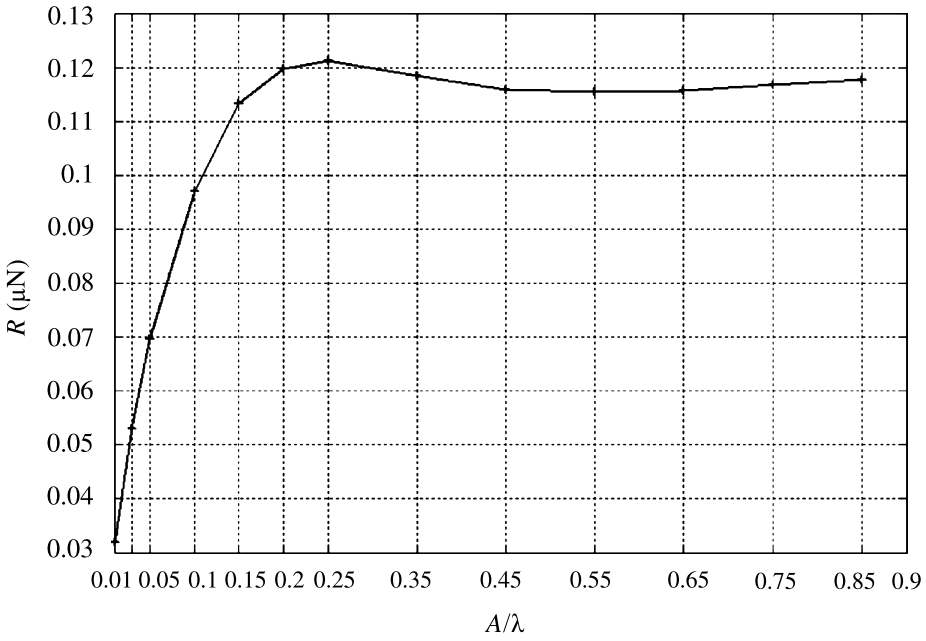

Figure 3. Reaction force per roughness peak R generated by the flattening of the surface asperities in the microscale model as a function of the amplitude to wavelength ratio A/λ of the initial asperity shape.

sonable for objects made of materials with substantially higher yield limit than the nickel base material of the gripper arm.

The initial and deformed shapes of the considered profiles are presented in Fig. 2. The reaction force per roughness peak generated by the imposed flattening of the asperities in the microscale contact simulations are depicted in Fig. 3. Note the non-linear variation of the response of the roughness peaks as a function of their shape. The elastic springback, i.e., the difference between the profile geometries at peak load and after unloading due to the elastic relaxation of the material, was analyzed for all considered geometries and was found to be small from the mechanical point of view.

2.3. A Simple Link between the Microscale and the Macroscale Contact Models

The results of the microscale model were obtained for a chosen crushing of the roughness profiles d_i, being a function of the initial amplitude A_i. Using a simple assumption the chosen flattening of the surface asperities can be shown to yield probably a lower bound to the real microscale deformation. Our purpose with the following approximate estimation is merely to verify that the resulting reaction forces from the microscale and from the macroscale models are in the same order of magnitude for the prescribed microscale flattening. The proposed method is thus not intended to correspond to a proper scale transition in the computational sense

(i.e., homogenization methods), but to verify that the macroscale and the microscale deformation states are consistent.

The essence of the verification is to check whether by filling uniformly the projected contact area A_{macro} obtained from the macroscale model with deformed sinusoidal roughness peaks of the microscale model at the prescribed crushing, the induced reaction force is of the order of magnitude of the macroscopic manipulating force (equation (3)).

$$F^{\Sigma}_{\text{micro}} = \sum_{A_{\text{macro}}} R_i = N_{\text{asperity}} \times R_i = \mathcal{O}(F_0^{\text{macro}}). \tag{3}$$

Note that the approximation of having a uniformly crushed surface roughness in the contact area A_{macro} limited by the macroscale contact radius corresponds to a cylindrical rigid flat punching of the rough surface with an imposed crushing d_i. Applying the above assumption to:

Case A, of the macroscale simulations (object–gripper contact mainly in the elastic domain), the overall reaction force $F^{\Sigma}_{\text{micro}} = [1.37\ \text{mN}, \ldots, 5.2\ \text{mN}]$ of the 4.3×10^4 deformed peaks filling the macroscopic contact area was in the same order of magnitude as the macroscopic manipulating force. This suggests that the assumed plastic deformation in the microscale contact problem matches the order of magnitude of the real plastic deformation of the roughness peaks. It is emphasized that the loading conditions in Case A (largest object held with the smallest manipulating force) are probably less severe than the practically used ones.

Case B (object–gripper contact showing mainly plastic response on the macroscale), the overall reaction force $F^{\Sigma}_{\text{micro}} = [50\ \text{mN}, \ldots, 190\ \text{mN}]$ of the 1.57×10^6 peaks filling the macroscopic contact area was lower than the macroscopic manipulation force. This means that the roughness peaks are crushed on average much more severely in reality than in the microscale model. This interpretation is confirmed by the deep penetration of the object of around 10 μm, calculated in the macroscale contact model. Consequently, considering the generally large contact stresses in the macroscale micromanipulation model, most of the surface asperities in the contact area can be assumed severely crushed. Unlike in the works reporting surface asperity persistence at considerably smaller relative penetration with respect to the height of the surface asperities (and sometimes in lubricated contact conditions) [38, 40, 43], in the micromanipulation setup considered the surface roughness is probably practically flattened, as in [44].

The force levels obtained from the microscale computation and upscaled by the considered simple cylindrical fiat punch assumption remained for all considered cases almost in the same order of magnitude as the macroscopic manipulation force. However, the assumed number of contact points in the contact zone with similar asperity densities as on a Si polycrystalline surface [5] was an order of magnitude larger than computed in [5], thereby resulting in an overall reaction force also an order of magnitude higher than one would expect considering the asperity density.

For a given macroscopically applied force, this means that the plastic deformation of the surface asperities in the microscale problem is most probably a lower bound with respect to the real micromanipulation setting, and the numerical results obtained can be considered to give a lower bound to the surface asperity flattening.

Note that in the case of a complete treatment of the scale transition additional computational difficulties would have to be considered. The interaction of the plastic behavior of the material with the frictional behavior of a small scale contact, involving features related to the dislocation activity in the material, may be of importance [45]. Such an interaction could indeed play a role in the behavior of a contact with the size considered here [46]. Moreover, the size effects related to high strain gradients in the material, potentially generated by the sharp variation in the geometry in the microscale contact, were recognized to have an influence on the response of the microscale contact. This phenomenon is taken into account in recent research works using higher-order strain gradient plasticity theories for example [47, 48]. Proper scale transition assumptions would allow extrapolating these effects to the higher scale contact behavior [49].

However, even though considering advanced contact and material constitutive laws would result in a more complete numerical representation, considering (i) the resulting complexity and (ii) the purpose and the investigated aspect of the contact response at the considered scales, it is not crucial for this level of comparison. Neglecting the aforementioned effects allowed the use of a relatively simple numerical model on the microscale defined by a limited number of parameters, corresponding to the ones used in the macroscale model. Probably some other assumptions related to the contact geometry of the proposed method could be investigated and potentially avoided to allow a deeper level of comparison (flat punch assumption on the macroscale, neglecting roughness asperity interaction).

3. Electrostatic Simulation on the Micro-level

The output of the microscale mechanical simulations (the deformed shapes of the roughness asperities) was used for the evaluation of the electrostatic adhesion force between the gripper and the object at the release of the manipulated object. At contact, some models (Johnson–Kendall–Roberts (JKR) [7, 50], Derjaguin–Muller–Toporov (DMT) [7, 51]) provide closed-form expressions for the adhesion force due to the interactions occurring in the contact area of rough elastic contacts. These theories are obviously no longer valid in the considered problem of micromanipulation which induces significant plastic deformation of the surface roughness on the gripper arm. Contact adhesion was evaluated in rough contacts of deformable objects in the plastic regime by semi-analytical methods, however making a perfectly plastic material assumption [32, 33].

To avoid these simplifying assumptions, the electrostatic computation was coupled (unilaterally) to the mechanical simulation of the elastic–plastic deformation

of the surface roughness using an experimentally measured hardening law of pure nickel. The electrostatic adhesion force was calculated for two conductors: the gripper arm made of pure nickel and the manipulated object.

Let us briefly recall the source and the governing physics of the electrostatic forces appearing in a contact. The thermodynamic equilibrium is the basis of the metal–metal contact theory [52]. When two dissimilar metallic objects are brought closer to each other, electrical interaction occurs before mechanical contact, charge transfer takes place when the separation distance of the order of 100 nm is reached due to the tunneling effect between the solids [53]. Each object acquires a certain amount of charges proportional to their contact potential difference U, related to the intrinsic properties of the materials and ranging generally from 0 V to 0.5 V [54]. In the practical case of micromanipulation the potential difference between the gripper and the manipulated object depends on the properties of the conducting materials considered as

$$U = \frac{W_1 - W_2}{e}, \tag{4}$$

where W (eV) is the work function which only depends on the nature of the metal and is governed by the Fermi level of the material, and e (C) is the electron charge. The electrical potential in the volume around the two conductors at different contact potentials obeys Laplace's equation.

$$\Delta U = 0. \tag{5}$$

The interface between the two conductors can be seen as a capacitor (equation (6)) on which the potential difference is imposed.

$$Q = \frac{\varepsilon_0 \varepsilon_r S}{z} U, \tag{6}$$

where Q (C) is the charge, z (m) stands for the separation distance and S (m^2) is the contact area, ε_0 (F/m) and ε_r are the permittivity of free space and the relative permittivity of the environment, respectively. When the separation distance between the two conductors is reduced, the electrostatic field $\vec{E}$ increases along with the number of charges Q on the surfaces.

$$\vec{E} = -\vec{\nabla} U, \tag{7}$$

where E (V/m) is the electric field obtained from the gradient of U. The result is an attractive (or repulsive) electrostatic pressure P_{el} (CV/m^3) between the gripper and the object.

$$P_{el} = \frac{\varepsilon_0 \varepsilon_r E^2}{2} \text{ with } E = \vec{E} \cdot \vec{n}, \tag{8}$$

with E (V/m) the electric field normal to the surface. The electrostatic force between two conductors are thus governed by the potential difference (materials), the permittivity (surrounding environment) and the area of contact (contact geometry).

In order to evaluate the electrostatic adhesion force in the rough surface model of the microscale mechanical simulations, the Comsol commercial finite element package was used to solve equation (5) with two-dimensional models. Each numerical model consisted of more than 21 000 degrees of freedom. The electrostatic simulation tool was validated in [12] using analytical models [10, 55, 56] and literature benchmarks [57, 58]. The simulations were performed at contact (in the beginning of the release), i.e., at a chosen separation distance of $z = 0.4$ nm (as in [54]) for the initial and the deformed profiles both at peak load and after unloading (Table 1). The same electrostatic computations were conducted for different separation distances. For all of them the obtained trends were found to be in good agreement with the results presented in the following.

3.1. Analysis of Electrostatic Forces

The numerical results are manifold considering the distribution of charges and the electrostatic force levels before and after the deformation of a roughness peak. The small magnitude of the electrostactic interaction forces with respect to the mechanical forces necessary to deform the asperities (Table 1) confirms the unilateral coupling of the electrostatic model to the microscale contact model. The results of the numerical model show physically sound trends, the magnitude of the electrostatic force increases with an increase in the applied voltage (Fig. 4), and with a decrease in the separation distance z.

Considering the influence of the initial shape of the studied profiles it was observed that the electrostatic force decreases with the increase of the amplitude A (for sharp geometries). The initial shape of the surface roughness has thus a significant influence both on the mechanical response to deformation (Fig. 2) and on the magnitude of the electrostatic force on the asperity surface (Fig. 4).

The main concern of this study, i.e., the variation of the electrostatic force as a consequence of the plastic deformation of the surface roughness, is considered in the following. The multiplicative factor γ between the electrostatic forces acting on the undeformed rough profile F_{init} and on the deformed profile F_{def} was found to be in the range

$$\gamma = \frac{F_{\text{def}}}{F_{\text{init}}} = [2, \ldots, 20] \tag{9}$$

for the considered cases depending on the ratio A/λ (Fig. 5). For the initially flattest peak the attractive electrostatic force before and after deformation was already doubled, and the most important increase was observed for the sharpest asperities (with increasing A/λ). The significant increase in the electrostatic adhesion force is related to the change in the distribution of the charges on the initial and on the deformed shape of the surface asperities (confirmed in the following section).

Figure 6 depicts the typical electrostatic force and charge distribution in the initial and in the deformed configuration (for profile number 5 of Table 1). The

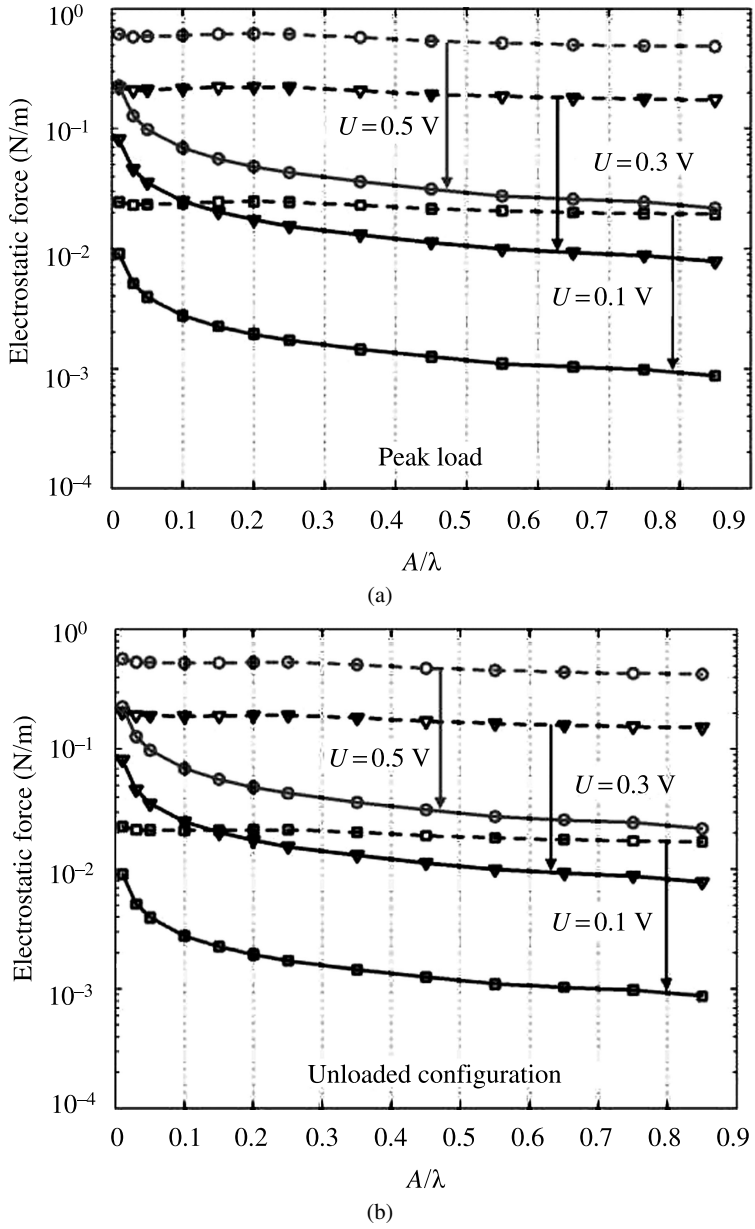

Figure 4. Results of the electrostatic simulation. Electrostatic adhesion force before (solid lines) and after deformation (dotted lines). Square marks stand for an applied voltage, of 0.1 V, triangle marks for 0.3 V and circle marks for 0.5 V. (a) For deformed shapes at peak load. (b) For the unloaded configuration.

electrostatic forces are concentrated at the peak of the undeformed asperity. The deformed shape, however, has a portion with an almost flat surface (plateau) where

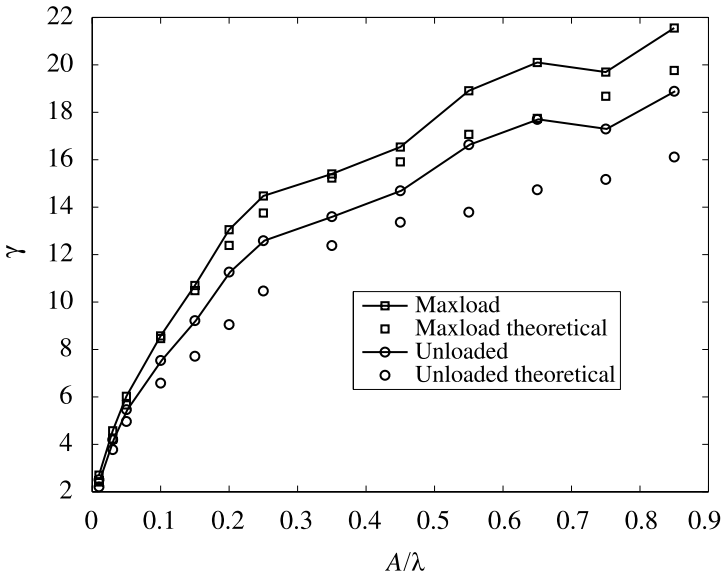

Figure 5. Variation of the multiplicative factor γ of the initial electrostatic force in the deformed configuration as a function of the amplitude to wavelength ratio A/λ of the initial asperity shape. Solid lines correspond to numerical results, non-interconnected symbols stand for the prediction of the closed-form expressions. Square symbols and circle symbols correspond to results at peak load (maxload) and in the unloaded configuration, respectively.

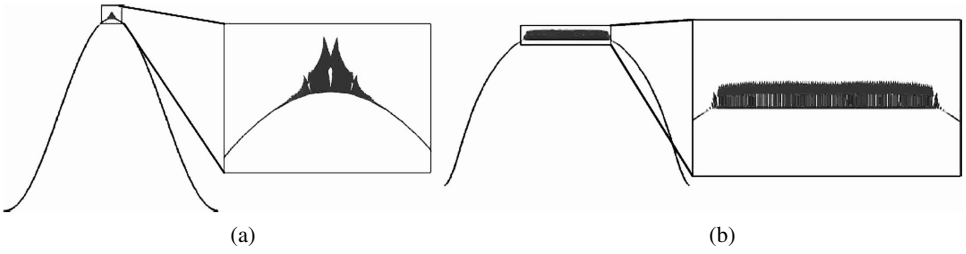

Figure 6. Charge and electrostatic force distributions in the undeformed (a) and in the deformed (b) configuration of the surface asperity profile number 5 in Table 1. In the undeformed configuration the charges are concentrated on the tip of the asperity, after deformation they are nearly uniformly distributed on the formed fiat surface.

the forces are uniformly distributed. Since electrostatic forces rapidly decrease with the separation distance, in the majority of cases the sides of the profile have almost no influence on the total electrostatic adhesion force. An exception was formed for blunt profiles with values of $A/\lambda < 0.01$ where the side effects cannot be neglected anymore. Consequently, the length of the formed plateau is a major parameter determining the overall electrostatic force in the deformed configuration.

3.2. Closed-Form Estimates for Electrostatic Forces

Considering the relatively simple charge and electrostatic force distributions in the initial and in the deformed configuration observed in the numerical model (Fig. 6) two closed-form expressions are proposed for the evaluation of the overall electrostatic adhesion force.

In the undeformed configuration, the sinusoidal profile has a curvature $c = A\omega^2$ which can be approximated by a circle of radius r

$$r = \frac{1}{A\omega^2} = \frac{\lambda^2}{4\pi^2 A}. \tag{10}$$

The electrostatic force acting on the sinusoidal profile was evaluated using an analytical approximation for a cylinder–plane contact [59]:

$$F_{\text{init}}\ (\text{N/m}) = \frac{\varepsilon_0 \varepsilon_r \lambda U^2}{\sqrt{32A}z^{3/2}}. \tag{11}$$

In the deformed configuration the analytical expression was derived from the model for contact between two infinite planes [10], adding the length of the plateau l as parameter:

$$F_{\text{def}}\ (\text{N/m}) = \frac{\varepsilon_0 \varepsilon_r U^2}{2z^2} l. \tag{12}$$

Taking the highest point of a roughness profile a_{top}, the plateau length l was defined by all the points within a vertical cutoff distance of 0.4 nm from a_{top}. Note that the unloaded profiles were slightly curved due to the elastic springback, a difference which influenced the resulting electrostatic forces, especially for the blunt asperities. The length of the plateau at peak load l_i^{peak} increases until $A/\lambda = 0.2$ and then decreases while the length of the plateau in the unloaded configuration l_i^{unload} taking into account the elastic springback globally decreases with increasing A_i/λ values (Table 1).

Figure 7 shows that the predictions of the numerical simulations and of the analytical expressions are in good agreement. The results of the closed-form expression in the initial configuration are more reliable for smaller than for larger A/λ ratios since the geometrical approximation of using a circle matches better the sinusoidal profiles in that case. The error is less than 10% for profiles with $A/\lambda < 0.4$.

There is less than 5% error for most A/λ ratios in the deformed configuration at peak load. The closed-form expression becomes unreliable only for $A/\lambda < 0.01$ due to side effects on the blunt profile (non-negligible contribution of the sides of the profile to the electrostatic force). The error is larger in the unloaded configuration due to the elastic springback because the calculation of the plateau length is less accurate in this configuration but the side effects are also more important. The good agreement between the results of the analytical expressions and of the numerical simulations in both cases confirms that for most profiles the presence of the plateau plays the significant role and the side effects can be neglected.

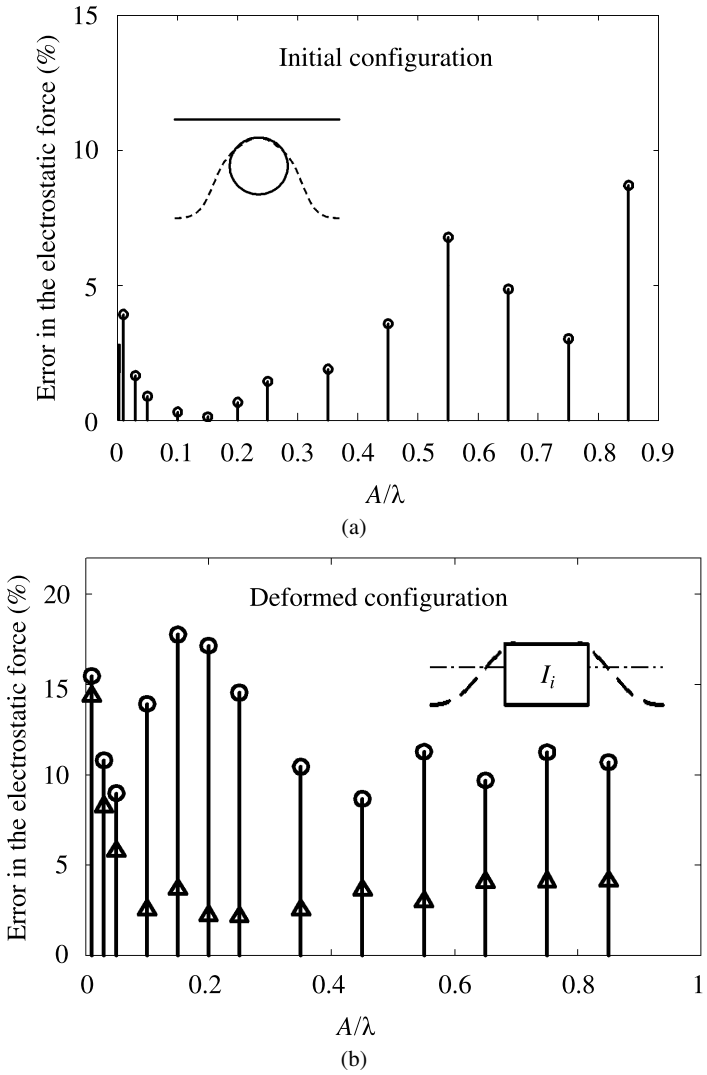

Figure 7. Percent error between the results of closed-form expressions and the numerical simulations. (a) For initial surface asperity shapes. (b) In the deformed configuration at peak load (triangle marks) and in the unloaded configuration (circle marks).

From the above closed-form approximations based on simple representations of the asperity geometry in the initial (cylinder–flat plane assumption) and in the deformed (flat segment–flat plane assumption) configurations it is possible to estimate the magnification factor γ of the electrostatic adhesion force if the shape of the initial profiles and the length of the plateau formed are known:

$$\gamma = \frac{2l}{\lambda}\sqrt{\frac{2A}{z}}. \tag{13}$$

The good correlation between the numerical results and the prediction of the closed-form expressions gives a graphical confirmation (Fig. 5) of our interpretation of the underlying physics of the studied source of potential release problems in micromanipulation by contact. The plastic deformation of the surface roughness on the deformable gripper arm (due to the macroscale manipulating force) results in the formation of plateaus on the peaks of the surface asperities. The presence of these plateaus changes the charge distribution on the contact surface leading to an increase in the electrostatic adhesion force in the contact.

Note that the application of the simple linking assumption (discussed in Section 2.3) showed that the imposed flattening of the surface asperities is probably a lower bound to the magnitude of the microscale deformation in the real micromanipulation setting. The degree of flattening of the surface roughness defines the length of the plateau formed on the peak of the surface asperities, which is directly related to the factor of increase in the electrostatic adhesion force. This underlines the fact as well that the computed γ is a lower bound to the real-life increase in the electrostatic contact adhesion due to the plastic flattening of the surface asperities during micromanipulation.

4. Conclusions and Perspectives

An important effect of the plastic deformation of the surface roughness on electrostatic contact adhesion was demonstrated using a semi-coupled multi-physics numerical model, since the initial electrostatic adhesion force on the asperities was magnified by a factor $\gamma = [2, \ldots, 20]$ after plastic deformation. The small magnitude of the electrostatic interaction forces with respect to the forces necessary to deform the surface asperities (Table 1) confirmed the validity of the assumption of unilateral coupling of the electrostatic model to the microscale contact model. The observed effect clearly contributes to the difficulty to release objects when the squeezing manipulation force is released. The key role of the fiat surface formed on the deformed profiles on the increase of electrostatic forces was identified and confirmed using a closed-form approximation of the electrostatic forces based on simplifying geometrical assumptions.

The obtained magnifying factor γ of the electrostatic adhesion force related to the plastic deformation effect seems to be merely a lower bound of the real-life increase. As pointed out before the higher contact point density (with respect to [5]) and the relatively small imposed flattening in the microscale model of $d_i = 2A_i/3$ give a lower bound to the magnitude of the deformation of the surface asperities with respect to the real micromanipulation setting. Moreover, in the case of real surfaces, considering the predictions of the numerical model used for the evaluation of the electrostatic forces, the charges would concentrate on the tip of asperities of the highest order roughness, thereby further decreasing the initial electrostatic forces. During deformation more than one level of asperities (considering the

protuberance-on-protuberance model) can be crushed [60] and γ could reach even higher values than the ones reported here.

These observations lead to the conclusion that decreasing the plastic deformation of surface asperities could substantially reduce release problems related to electrostatic adhesion force in micromanipulation by contact (e.g., application of coatings with specific elastic behavior), which is a useful information for the design of such devices.

In the presented study only the electrostatic adhesion force was computed to focus on its particular effect, the other contributions to the adhesion force were not considered in this first approach. This allowed to study the semi-coupled mechanical and electrostatic problems. In future works a specific effort will be devoted to perform a similar coupling of van der Waals and capillary forces to the proposed mechanical problem. This would at that stage allow comparing work of adhesion and surface energy quantities with experimental results. Indeed, since the work of adhesion and surface energy quantities generally correspond to a more general definition of adhesion measured experimentally [1] including all potential contributions, they cannot be computed from the presented numerical results. The long term goal thus is to group the results obtained for these three forces in order to evaluate the influence of the plastic deformation of surface asperities on contact adhesion in a more global sense. These numerical results could then be compared to the prediction of classical theories of contact adhesion, which defines a complementary research direction and even to experimental data, which would be particularly interesting.

Acknowledgement

This work was sponsored by the Communauté Française de Belgique within the framework of an Action de Recherche Concertée (convention 04/09-310).

References

1. K. Komvopoulos, *J. Adhesion Sci. Technol.* **17**, 477–517 (2003).
2. M. Zhao, W. S. Slaughter, M. Li and S. X. Mao, *Acta Mech. Sin.* **51**, 4461–4469 (2003).
3. L. Kogut and K. Komvopoulos, *J. Appl. Phys.* **94**, 6386–6390 (2003).
4. R. W. Carpick, J. R. Van Langedon, E. H. Wilson and K. Sridharan, in: *Proc. of the SEM VII International Congress and Exposition on Experimental and Applied Mechanics*, Portland, USA, p. 725 (2001).
5. R. W. Carpick, E. E. Flater, J. R. Van Langendon and M. P. de Boer, in: *Proc. of the SEM VIII International Congress and Exposition on Experimental and Applied Mechanics*, Milwaukee, USA, p. 282 (2002).
6. P. Lambert, *Capillary Forces in Microassembly: Modeling, Simulation, Experiments, and Case Study*. Springer (2007).
7. C. M. Mate, *Tribology on the Small Scale*. Oxford University Press (2008).

8. J. N. Israelachvili, *Contemporary Phys.* **15**, 159–177 (1974).
9. P. Lambert and S. Régnier, *J. Micromechatronics* **3**, 123–157 (2006).
10. R. S. Fearing, in: *Proc. of IEEE/RSJ Conf. on Intelligent Robots and Systems*, Pittsburgh, USA, p. 212 (1995).
11. B. Bhushan, *J. Vac. Sci. Technol. B* **21**, 2262–2296 (2003).
12. M. Sausse Lhernould, A. Delchambre, S. Régnier and P. Lambert, *Appl. Surf. Sci.* **253**, 6203–6210 (2007).
13. Y. I. Rabinovich, J. J. Adler, A. Ata, R. K. Singh and B. M. Moudgil, *J. Colloid Interface Sci.* **232**, 10–16 (2000).
14. S. Herminghaus, *Phys. Rev. Lett.* **95**, 264301 (2005).
15. J. Agnus, C. Clévy, Y. Urushima and R. Perez, in: *Proc. of the 35th Int. Symposium on Robotics*, Paris, France (2004).
16. I. Kovács and G. Vörös, *Int. J. Plast.* **12**, 35–43 (1996).
17. *ASM Handbook: Properties and Selection: Nonferrous Alloys and Special-Purpose Materials*, Vol. 2. Materials Park, Ohio (1990).
18. R. C. Weast (Ed.), *CRC Handbook of Chemistry and Physics*, 62nd ed. CRC Press, Boca Raton, FL (1981).
19. R. B. Ross, *Metallic Materials Specification Handbook*, 4th ed. Springer (1992).
20. A. Nayer, *The Metals Databook*. McGraw-Hill (1997).
21. F. Dalla Torre, H. Van Swygenhoven and M. Victoria, *Acta Mater.* **50**, 3957–3970 (2002).
22. P. Alart and A. Curnier, *Comp. Meth. Appl. Mech. Eng.* **92**, 353–375 (1991).
23. J. P. Ponthot, *Int. J. Plast.* **18**, 91–126 (2002).
24. H. Hertz, *J. Reine und Angewandte Mathematik* **92**, 156–171 (1882).
25. I. Sevostianov and M. Kachanov, *J. Mech. Phys. Solids* **56**, 1380–1400 (2008).
26. M. Ciavarella, S. Dibello and G. Demelio, *Int. J. Solids Struct.* **45**, 879–893 (2008).
27. T. Bell, K. Mao and Y. Sun, *Surf. Coat. Technol.* **108–109**, 360–368 (1998).
28. J. A. Greenwood and J. B. P. Williamson, *Proc. R. Soc. Lond. A* **295**, 300–319 (1966).
29. C. K. Bora, M. E. Plesha, E. E. Flater, M. D. Street and R. W. Carpick, in: *Proc. of the 2004 ASME/STLE Joint International Tribology Conference*, Long Beach, California (2004).
30. C. K. Bora, E. E. Flater, M. D. Street, J. M. Redmond, M. J. Starr, R. W. Carpick and M. E. Plesha, *Tribal. Lett.* **19**, 37–48 (2005).
31. R. Buzio, C. Boragno and U. Valbusa, *Wear* **254**, 917–923 (2003).
32. T.-Y. Zhang, W.-H. Xu and M.-H. Zhao, *Acta Mater.* **52**, 57–68 (2004).
33. J. L. Liou and J. F. Lin, *J. Appl. Mech.* **74**, 603–613 (2007).
34. M. Nosonovsky and G. G. Adams, *J. Tribal.* **122**, 490–495 (2000).
35. F. Robbe-Valloire, B. Paffoni and R. Progri, *Mech. Mater.* **33**, 617–633 (2001).
36. R. L. Jackson and J. L. Streator, *Wear* **261**, 1337–1347 (2006).
37. M. Kostoglou and A. J. Karabelas, *J. Colloid Interface Sci.* **171**, 187–199 (1995).
38. J. Jamari and D. J. Schiper, *Wear* **262**, 138–145 (2007).
39. A. K. Nanda Kumar, M. D. Kannan, S. Jayakumar, K. S. Rajam and V. S. Raju, *Surf. Coat. Technol.* **201**, 3253–3259 (2006).
40. J. Larsson, S. Biwa and B. Strøakers, *Mech. Mater.* **31**, 29–41 (1999).
41. M. Ciavarella, V. Delfine and V. Demelio, *Wear* **261**, 556–567 (2006).
42. L. Nicola, A. F. Bower, K.-S. Kim, A. Needleman and E. Van der Giessen, *J. Mech. Phys. Solids* **55**, 1120–1144 (2007).
43. P. K. Rajendrakumar and S. K. Biswas, *Tribal. Lett.* **3**, 297–301 (1997).

44. A. Azushima, S. Kuba, S. Tani and D. D. Olsson, *Wear* **260**, 258–264 (2006).
45. J. A. Hurtado and K.-S. Kim, *Proc. Roy. Soc. Lond. A* **455**, 3363–3384 (1999).
46. V. S. Deshpande, D. S. Balint, A. Needleman and E. Van der Giessen, *Modell. Simul. Mater. Sci. Eng.* **15**, 97–108 (2007).
47. K. K. Tho, S. Swaddiwudhipong, J. Hua and Z. S. Liu, *Mater. Sci. Eng. A* **421**, 268–275 (2006).
48. R. K. Abu Al-Rub, *Mech. Mater.* **39**, 787–802 (2007).
49. I. Temizer and P. Wriggers, *Comput. Methods Appl. Mech. Eng.* **198**, 377–396 (2008).
50. K. L. Johnson, K. Kendall and A. D. Roberts, *Proc. R. Soc. Lond. A* **324**, 301 (1971).
51. B. V. Derjaguin, V. M. Müller and Y. P. Toporov, *J. Colloid Interface Sci.* **53**, 314–326 (1975).
52. W. Harper, *Contact and Frictional Electrification*. Oxford at the Clarenton Press (1967).
53. J. Lowell and A. Akande, *J. Phys. D: Appl. Phys.* **8**, 53–63 (1975).
54. R. A. Bowling, in: *Particles on Surfaces 1: Detection, Adhesion and Removal*, K. L. Mittal (Ed.), pp. 129–142. Plenum Press, New York, NY (1986).
55. H.-J. Butt, B. Cappella and M. Kappl, *Surf. Sci. Rep.* **59**, 1–152 (2005).
56. S. Hudlet, M. Saint Jean and J. Berger, *Eur. Phys. J. B* **2**, 5–10 (1998).
57. H. W. Hao, A. M. Baro and J. J. Saenz, *J. Vac. Sci. Technol. B* **9**, 1323–1328 (1991).
58. G. M. Sacha, A. Verdaguer, J. Martinez, J. J. Sáenz, D. F. Ogletree and M. Salmeron, *Appl. Phys. Lett.* **86**, 123101 (2005).
59. W. R. Smythe, *Static and Dynamic Electricity*. McGraw-Hill (1968).
60. Y.-F. Gao and A. F. Bower, *Proc. R. Soc. A* **462**, 319–348 (2006).